Space of solutions to ocean surface wind measurement using scatterometer constellations

Patrick Walton
David Long

Space of solutions to ocean surface wind measurement using scatterometer constellations

Patrick Walton* and David Long
Brigham Young University, Department of Electrical and Computer Engineering,
Provo, Utah, United States

Abstract. Satellite wind vector data are integral to atmospheric models and forecasts, but current measurement limitations make some synoptic, mesoscale activities difficult to observe. Using miniaturized electronics and advanced deployable mechanisms, new satellite wind scatterometers may be possible that increase spatial, temporal, and wind resolution and coverage. We propose a simple parametric model of the space of satellite wind scatterometer designs, their performances, and the transformation between design and performance, together called a solution space model. We explore two applications of this model: understanding how advances have expanded the design space and searching for alternative approaches to satellite wind scatterometry. Recent advances enable a greater capability-to-volume ratio, which enables constellations of small, low-cost scatterometers that co-operate in a variety of modes. We present two example concepts for constellations of co-operative satellite wind scatterometers. We estimate that a constellation of CubeSat scatterometers may affordably measure global ocean vector winds every three hours. © *2019 Society of Photo-Optical Instrumentation Engineers (SPIE)* [DOI: 10.1117/1.JRS.13.032506]

1 Introduction

Satellite scatterometers produce microwave Earth-observation data well-suited for measurement of numerous geophysical properties,[1] including wind speed and direction (wind vectors) near the ocean surface, ice coverage, vegetation coverage, soil moisture, and average wind vectors over sand and snow.[2–6] Measurement of wind vectors near the ocean surface is especially important for refining global scientific models of weather and climate processes. More accurate models enable more reliable forecasting, which provides value to various sectors dependent on accurate weather information, including industry, agriculture, water management, transportation, and tourism.[7]

Satellite scatterometers have overwhelming advantages over *in-situ* measurement systems, such as instrumented ships and buoys, due to their ability to measure wind vectors globally. However, scatterometers are currently limited to spatial resolutions of tens of kilometers, temporal resolutions of multiple days, wind speed resolutions of multiple meters per second, and wind direction resolutions of tens of degrees. These resolutions represent improvements over early scatterometers, described in Sec. 2. However, the majority of improvements have been incremental, applied to individual subsystems only. In Sec. 3, seeking system-level improvements, we develop a parametric model of the space of satellite wind scatterometer designs, their performances, and the transformation between design and performance, collectively called a solution space model. In Sec. 4, we explore two applications of the design space including evaluation of the growth of the achievable design space and exploration of potential alternative approaches to satellite wind scatterometry.

---

*Address all correspondence to Patrick Walton, E-mail: m.patrick.walton@gmail.com

2 Background

Scatterometry is an important application of radar remote sensing, most prominently applied in global wind vector measurement. Its fundamentals and history provide insight into the solution space of satellite wind scatterometry. Experimentation and development between 1970 and 2000 established two primary design architectures for satellite scatterometry: the fanbeam and the scanning-pencil beam.[1] More recently, a hybrid design, the rotating fan beam scatterometer, has been developed.[8]

2.1 *Ocean Surface Vector Wind Scatterometry*

Scatterometers are active microwave radars used to infer surface properties by measuring the fraction of the surface-scattered signal returned to the radar receiver, known as the radar cross-section. Radar cross-section is formally defined as $\sigma = P_r/P_t$, where P_r is the power reflected from the target and P_t is the transmit power illuminating the target. The normalized radar cross-section, σ_0, is the key characteristic of the response of a surface to radar reflections, defined as $\sigma_0 = \sigma/(\Delta x \Delta y)$, where $\Delta x \Delta y$ is the area of the resolution cell.[1]

The received signal can be used to determine wind speed and direction.[1,3] Atmospheric wind flow creates stress at the surface of the ocean. This results in waves with size corresponding to the strength of the associated wind. These waves scatter signals according to Bragg scattering. The scatter broadens with increasing wind speed and varies sinusoidally with the angle between the look direction and the wind direction (see Fig. 1).

The relationship between σ_0 and wind vector is described by the geophysical model function (GMF), expressed as $\sigma_0 = f(|U|, \chi, \theta, \lambda, pol, \dots)$, where $|U|$ is the wind speed, θ is the observation incidence angle [Fig. 1(a)], λ is the radar wavelength, pol is the radar polarization, and ". . ." represents neglected variables. The azimuth angle between the look direction and the wind direction is $\chi = \gamma - \Phi$, where γ is the look direction [Fig. 1(a)] and Φ is the wind direction, both measured from North. Typically, the GMF is empirically developed, inverted, and tabulated for use in the wind retrieval process.[9,10]

With a single σ_0 measurement, the GMF has infinite wind vector solutions, due to the sinusoidal variance of σ_0 with χ [see solid line in Fig. 1(b)]. With two, collocated, near-simultaneous measurements, the GMF has four solutions, indicated by the black arrows in Fig. 1(b). Obtaining a unique solution [black circle in Fig. 1(b)] requires at least three measurements taken from diverse azimuth look angles. In practice, additional processing is required to select a single direction due to noise and the near-symmetry of the GMF at χ separations of 180 deg.
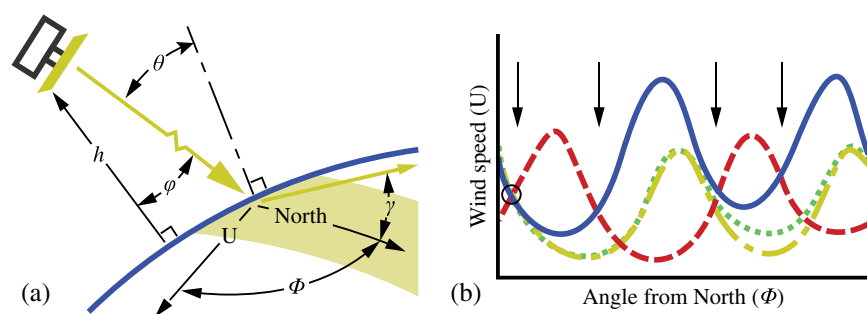
Fig. 1 (a) Wind vector measurement geometry. Incidence angle, θ, is measured from the surface normal to the look direction. Azimuth look angle, γ, is measured from the North to the surface projection of the look direction. Φ is the wind direction measured from North, and U is the wind speed. Orbital altitude, h, is measured from the nadir point to the spacecraft, and look elevation angle, ϕ, is measured from the altitude line to the look direction. (b) Wind vector solution space.[2] Each line represents the possible solutions for a single, noise-free σ_0 measurement, obtained at the following azimuth look angles and polarizations using the NSCAT-1 GMF; blue/solid: 45 deg, v-pol; red/dashed: 135 deg, v-pol; yellow/dash-dot: 65 deg, v-pol; green/dotted: 65 deg, h-pol. Black arrows mark the four solutions of the 45 deg and 90 deg σ_0 measurements. The small circle at left indicates true wind speed and direction.
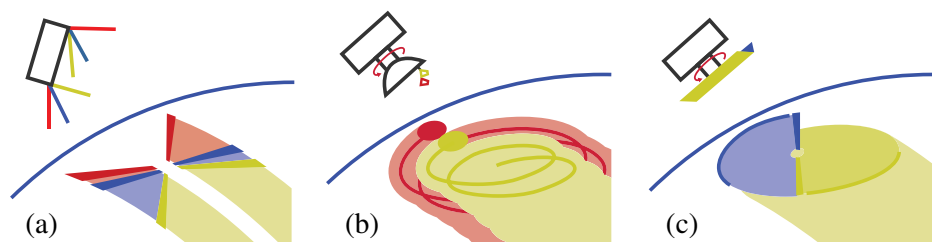
2.2 *Conventional Approaches*

The first satellite scatterometer, RADSCAT on Skylab, was unable to resolve individual wind vector measurements with its single dish antenna but successfully detected variance in physiography by measuring the scattered signal.[11] SASS on SeaSat measured wind vectors with two fan-beam antennas per swath, but complicated postprocessing was required to reduce the ambiguities in SASS wind data.[12]

Europe's ESCAT scatterometer on the ERS-1 and ERS-2 satellites and NASA's NSCAT scatterometer on the ADEOS-1 satellite demonstrated unambiguous wind vector measurement using three fan-beam antennas per swath [Fig. 2(a)], on-board digital processing to subdivide the swath, and collocation of σ_0 measurements to form wind vector cells on the ground.[2,13] NASA's SeaWinds on QuikSCAT demonstrated wind vector measurement by circularly scanning two offset pencil beams[14] [Fig. 2(b)]. Subsequent scatterometers, flown by Europe (ASCAT), India (OSCAT), and China (HY-2a), have been patterned after and improved on these established approaches.[3] For example, the ASCAT instruments, aboard Europe's MetOp satellites, improve on the ESCAT instruments with continuous operation, a doubled swath, greater sensitivity, and finer wind vector resolution.[15] In 2018, China and France launched CFOSAT to demonstrate the rotating fan beam [Fig. 2(c)], which combines the approaches of the fan beam and scanning pencil beam.[8]

The antenna beam shape and corresponding ground swath pattern are the defining characteristic of each approach. The antennas, resulting footprint, scanning, and ground swath of each of the conventional approaches are shown in Fig. 2. Fan-beam scatterometers scan like angled push-brooms on the ground requiring long, rectangular antennas [Fig. 2(a)]. Scanning pencil-beam scatterometers cover concentric helices on the ground using rotating, dish antennas [Fig. 2(b)]. Rotating fan beam scatterometers scan like a lawnmower on the ground, covering concentric helices with long, rotating, rectangular antennas [Fig. 2(c)].

Each approach has tradeoffs, especially in the antenna, wind retrieval, and swath. Fan-beam antennas are difficult to stow, deploy, and calibrate, but they are more reliable after deployment. Scanning pencil-beam dish antennas are compact and stable, but they require rotary bearings, which are liable to fatigue. Scanning pencil beam scatterometers typically have greater signal-to-noise ratio (SNR) than fan beam scatterometers, but they have shorter dwell time due to scanning. Rotating fan beams generally combine the challenges of the above tradeoffs.

While fan-beams illuminate the surface at a large range of incidence angles, scanning pencil beams observe at a couple of incidence angles only. A complete GMF must be developed for each incidence angle, so scanning pencil beams require less effort in model development. Scanning pencil-beam and rotating fan beam scatterometers provide valuable measurements in the nadir region, where fan-beam scatterometers have a gap, because their measurements would have incidence angle less than the minimum allowable 18 deg. The rotating fan beam may provide greater wind direction accuracy since it acquires more near-simultaneous, azimuth-diverse measurements.[8]

(a)   (b)   (c)

Fig. 2 Illustration of the conventional approaches to satellite wind scatterometry, including the antennas, scanning, footprint, and ground swath of each. (a) Fan-beam scatterometer (NSCAT). (b) Scanning pencil-beam scatterometer (SeaWinds). (c) Rotating fan-beam scatterometer (RFSCAT).
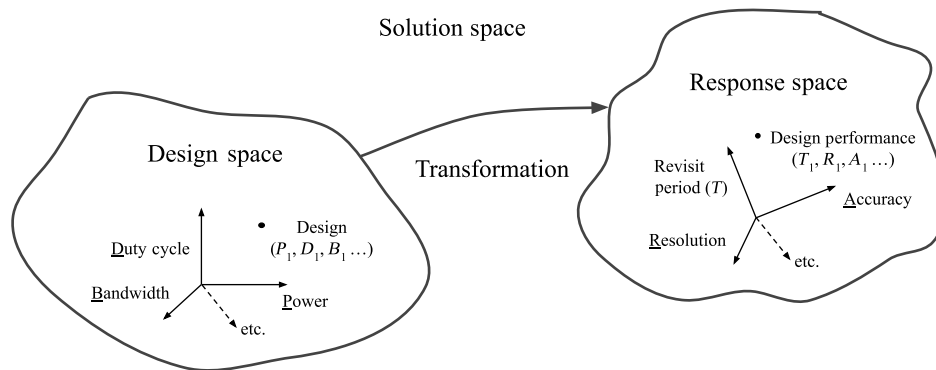
Fig. 3 Illustration of the solution space concept. The solution space includes the design space required to accomplish some system objective and the response space describing how well the design meets that objective. It also includes the transformation between the design space and the response space.

3 Development of the Solution Space Model for Satellite Wind Scatterometry

The technologies required for satellite wind scatterometry have advanced significantly in recent years, but little attention has been paid to the overall measurement approach. We expect combinations of advanced technologies, especially miniaturized electronics and advanced deployable mechanisms, to enable measurement approaches with improved spatial, temporal, or wind vector resolutions. We develop the solution space model to gain deeper understanding of the space of possible scatterometer systems that can measure ocean vector winds.

The solution space consists of a design space, a response space, and the transformation between them. This relationship is shown in Fig. 3. In Sec. 3.1, we structure the solution space model by defining the parameters that make up the design space and the response space. In Sec. 3.2, we develop the transformation between the design space and the response space by expressing the response parameters as functions of the design parameters. We verify this transformation using past scatterometers. This approach is adapted from the design approach of Mattson and Sorenson.[16]

3.1 Structure of the Solution Space Model

The solution space model is composed of a design space and a response space (Fig. 3), which we treat as linear spaces. Solution space model development involves identification of a basis for each space and the transformation between the design space and response space. The dimensions spanned by the design basis are the parameters over which the designer has direct control. The dimensions spanned by the response basis are the parameters that characterize system performance. Response parameters for satellite wind scatterometry include spatial resolution, spatial range (daily coverage), temporal resolution (revisit period), wind vector resolutions (accuracy), and wind dynamic range. Estimation of wind measurement accuracy and dynamic range is complicated, so we substitute these with proxy response parameters. Our response basis for satellite wind scatterometry is given in Table 1.

We use the approximations of the response parameters, the transform equations, to identify key design parameters. Where possible, we simplify the transform equations to reduce the number of dimensions in the design space. The final design basis is given in Table 2. This approach removes several parameters that are fully dependent on the key design parameters. These intermediate parameters, given in Table 3, simplify the transformation equations in Sec. 3.2. However, due to their dependency on the design parameters, they do not provide additional information to the design.

In practice, the accessible region of the design space is limited by the state-of-the-art of technology required for satellite wind scatterometry. To prevent premature downselection, estimates of accessible ranges included in Table 2 are based on first principles and precedent, even though extreme values may result in poor performance.

Table 1 Response basis of satellite wind scatterometers.

Response dimension	Ideal range	Transform	Contributing design parameters[a]
Normalized standard deviation[b,c] (K_{pc})	<0.5	Eq. (1)	$P_t, \tau, D_r, T_d, \lambda, B, \phi, L_e, h, N_s, F_s$
Incidence angle[c] (θ)	18 deg to 60 deg	See Table 3	ϕ, h
Wavelength[b,c] (λ)	2.1 or 5.7 cm	λ	λ
Polarization[b] (*pol*)	N/A	*pol*	*pol*
Near-simultaneous, azimuth-diverse looks[b] (N_L)	2 to 3+	Eq. (2)	$T_d, \phi, L_{ex}, \lambda, h, N_s, N_a, F_f, \omega$
Spatial resolution (Δxy)	0 to 25 km	Eq. (3)	$T_d, \lambda, B, \phi, h, F_s$
Daily coverage (D)	>0.7	Eq. (4)	$\lambda, L_{ex}, h, I, N_s, \psi_x, W_s, D_o, F_f, S$
Revisit period (T_r)	<24 h	Eq. (5)	$h, N_a, \psi, \phi, \lambda, L_e N_{op}, S,$

[a]Defined in Table 2.
[b]Proxy for wind measurement accuracy.
[c]Proxy for wind measurement dynamic range.

3.2 *Transformation between the Design Space and the Response Space*

The approximations for the response parameters define a transformation between the design space and the response space, which allows the designer to rapidly evaluate a large variety of designs. We proceed to briefly describe each response approximation. For existing approximations, we describe our adaptation, intended to reduce design dimensions. For our own approximations, we describe our derivation and the associated assumptions. For approximations to proxy response parameters, we also describe the relationship between the proxy and wind vector resolution. To simplify discussion of lengthy approximations, we introduce intermediate parameters and give their equations and derivations in Table 3.

We begin with normalized standard deviation of the σ_0 measurements, K_{pc}, which is the primary determinant of wind measurement dynamic range and accuracy. Our approximation is developed by substituting $\tau = T_d D_r$ into the expression for K_{pc} given by Ulaby and Long,[1] where τ is the pulse length. $F_s N_s[sup]N_s[syn]$ is also supplemented for N_{looks}. The resulting equation for K_{pc} is

$$K_{pc} \approx \frac{1}{\sqrt{F_s N_s[sup]N_s[syn]T_d D_r B[Tx]}} \sqrt{1 + \frac{2}{S_N} + \frac{1}{S_N^2}}, \tag{1}$$

where $F_s, N_s, T_d, D_r,$ and B are design parameters defined in Table 2, and S_N is an intermediate parameter defined in Table 3. $N_s[sup]$ and $N_s[syn]$ are subparameters of N_s, defined in greater detail in Sec. 4.2. $N_s[sup]N_s[syn]T_d D_r B$ is the time-bandwidth product of $N_s[sup]N_s[syn]$ co-operative instruments, with F_s measurements combined for greater quality.

Incidence angle, θ, increases scatter dynamic range as the projection of the ocean surface waves along the line-of-sight grows.[1] Typically, measurements must have an incidence angle greater than 18 deg and less than 60 deg to be usable in wind retrieval. Incidence angle is both a response dimension and an intermediate parameter, so its transformation is provided in Table 3.

Wavelength, λ, is both a design parameter and a response parameter, so no transformation is necessary. Wavelength directly impacts dynamic range and accuracy as higher wavelengths are more readily attenuated by rain. GMFs exist for C-band (5 cm) and Ku-band (2 cm). These wavelengths are typical because of the cost and risk involved in developing new GMFs.

The number of near-simultaneous, azimuth-diverse looks, N_L, impacts wind retrieval as described in Sec. 2.1. For the nonscanning case, N_L is the product of supplementary and synergistic satellite antenna quantity and supplementary satellite quantity. Synergistic satellites may increase this by a factor of $N_s[syn](N_s[syn] + 1)/2$, as described in Sec. 4.4. If the instrument scans, we multiply by the number of scans per footprint. We assume that looks are adequately

Table 2 Design basis for satellite wind scatterometers.

Design dimension	Estimated accessible range	Notes
Transmit power (P_t)	0 to 5 kW +	Max P_t is based on the solar power generated by the International Space Station (ISS).
Pulse length (τ)	5 to 50 ms	
Radar duty cycle (D_r)	0 to 1	$D_r = \tau/PRI$, where τ is the pulse length and PRI is the pulse repetition interval.
Dwell time (T_d)	0 to Δt_{rs}	$T_d = n_p PRI$, where n_p is the number of coherently integrated pulses. Δt_{rs} is in Table 3.
Wavelength (λ)	6 mm to 5 m	Accessible range limited by Bragg scattering.
Polarization (pol)	Any	Linear polarization is typical.
Bandwidth $\begin{pmatrix} \text{Transmit} & B[Tx] \\ \text{Receive} & B[Rx] \end{pmatrix}$	$\dfrac{c}{1000\lambda}$ to $\dfrac{c}{10\lambda}$	$B[Tx] = 1/\tau$ for interrupted continuous wave, $B[Tx]$ is the chirp bandwidth for frequency modulated signal, and $B[Tx] = 1/\tau_{\text{chip}}$ for phase-coded signal.
Look elevation angle (ϕ)	0 to $\sin^{-1}\left(\dfrac{R_E}{R_E + h}\right)$	The upper bound on ϕ range points to the horizon. $\phi_{\max}$ corresponds to $\theta_{\max}$ (see Table 3).
Effective antenna length (L_e[a])	$\dfrac{\lambda}{4}$ to 22 m +	$L_e = \eta_e \sqrt{\eta_a} L$, where η_a is the aperture efficiency, η_e is the antenna efficiency, and L is the antenna length. Upper L_e bound is taken as size of ISS.
Orbit altitude (h)	100 to 1,500,000 km	Maximum h is taken as the maximum Earth orbit, or the distance to Earth-Sun L1.
Orbital plane quantity (N_{op})	1 to $N_s[comp]$[b]	$N_s[comp]$ is defined in Sec. 4.1.
Orbit inclination (I)	0 to $\dfrac{\pi}{2}$	Inclination is mapped to a limited range to simplify coverage approximation.
Orbit duty cycle (D_o)	0 to 1	$D_o = T_o/T_s$, where T_o is the operational time per orbit and T_s is given in Table 3.
Satellite quantity (N_s[b])	1 to 300 +	Upper N_s is based on the largest constellation launched at time of this writing.
Antenna quantity (N_a[b])	1 to 20 +	Upper N_a is based on the number of feeds on a GPS satellite.
Focus factor (F_f)	0 to $\Delta t_{rs}\omega$	$F_f = P_o/P$ where P_o is the observed subsatellite path and P is the total subsatellite path.
Scan Angle (ψ[a])	0 to $\phi_{\max}$	
Downsampling factor (F_s)	0 to $N_{\text{WVC min}}$	$N_{\text{WVC min}} = \min(a_x/\Delta x, a_y/\Delta y)$
Scan rotation rate (ω)	0 to 10 Hz+	

[a]Subscript x and y denote cross-track and along track, respectively.
[b]Bracketed subparameters, $N_s[\ldots]$ and $N_a[\ldots]$, are described in Sec. 4.2.

collocated on the ground and that orbital plane has an equal number of satellites and each antenna has an equal number of polarizations. Thus, an approximate relationship for N_L is

$$N_L \approx N_a[sup]N_a[syn]N_s[sup]N_s[syn](N_s[syn] + 1)F_f \, \max\left(1, a_y \frac{\omega T_s}{2\pi R_E}\right), \qquad (2)$$

where N_s, N_a, F_f, and ω are design parameters defined in Table 2. $N_s[sup]$ and $N_s[syn]$ are subparameters of N_s, defined in greater detail in Sec. 4.2. Likewise, $N_a[sup]$ and $N_a[syn]$ are subparameters of N_a. a_y and T_s are intermediate parameters defined in Table 3.

Table 3 Equations and derivations of intermediate parameters.

Parameter equation	Notes
$S_N = \dfrac{P_t\sqrt{\tau D_r T_d}\,L_{ex}^2 L_{ey}^2 \sigma_0 \Delta_x \Delta_y \eta_e^2 B[Tx]}{4\pi R_s(\theta_{avg})^4 \lambda^2 k T_0 F L_s B[Rx]}$	*SNR:* Adapted from the radar equation given in Ref. [17]. σ_0, F, η_e, and L_s are assumed. k (Boltzmann) and $T_0 = 290$ K are constant.
$\theta = \sin^{-1}\left(\dfrac{R_E + h}{R_E}\,\sin\phi\right)$	*Radar incidence angle:* Derived using a spherical Earth assumption and the law of sines. θ_{avg} is the average angle across the scan pattern. θ_{max} is the maximum angle that produces quality measurements.[2] $R_E^{\,a}$ is a constant. c is the speed of light.
$\Delta x, \Delta y \approx \begin{cases} \dfrac{c\cos\theta_{avg}}{2B[Tx]}; \\ a_x; \\ \dfrac{\lambda h}{2 v_s T_d \cos\theta_{avg}} \end{cases}$	*Spatial resolution:* Ground projection of radar range resolution given in Ref. [17]; footprint if timing resolution used; or Doppler resolution derived from Eq. 13.26 given by Ulaby,[1] assuming $(x+dx)^2 + (y+dy)^2 \approx x^2 + y^2 = h^2\tan^2\theta\cos^2\gamma + h^2\tan^2\theta\sin^2\gamma = h^2\tan^2\theta$, where γ is the azimuth look angle measured from North.
$\theta_3 = \dfrac{\alpha_a \lambda}{L_e}$	*3 dB beamwidth:* For θ_{3x}, cross-track beamwidth, substitute L_{ex}. For θ_{3y}, along track beamwidth, substitute L_{ey}.[17] α_a, the beamwidth factor, is assumed.
$\alpha = \theta - \phi$	*Earth angle:* Spherical Earth assumption.
$R_s = R_E \sin\alpha / \sin\theta$	*Slant range:* Derived using law of sines. $R_E^{\,a}$ is constant.
$a_x \approx \dfrac{R_s \theta_{3x}}{\sin\theta}$	*Cross-track footprint width:* Arc-length approximately projected on the ground. $a(\theta_{max})$ is the footprint width at swath's edge.
$a_y \approx R_s \theta_{3y}$	*Along-track footprint width:* Small angle approximation.
$A_f = a_x a_y$	*Antenna footprint area:* Square footprint approximation.
$W_s \approx N_a[\text{comp}]\left[\dfrac{R_s \psi_x}{\sin\theta_{avg}} + a(\theta_{max})\right]$	*Swath width:* Independently scanning antenna groups and complementary satellites in the same orbit, multiplied by the sum of cross-track scan arc-length (approximately projected on the ground) and the swath-edge footprint.
$\Delta t_{rs} = \dfrac{\alpha(\theta_{max}) T_s}{2\pi}$	*Rescan window:* Maximum time available to rescan the same swath area, based window of observation within allowable incidence angle.
$v_s = \sqrt{g_s R_E^2 / (R_E + h)}$	*Satellite velocity:* Elachi et al.[18] $g_s^{\,b}$ and $R_E^{\,a}$ are constant.
$T_s = 2\pi(R_E + h)/v_s$	*Satellite orbital period:* Elachi et al.[18] $R_E^{\,a}$ is constant.
$S = 2\pi R_E \dfrac{T_s}{T_E}$	*Orbit step:* Adapted from Elachi et al.[18] by replacing 360 deg with $2\pi R_E$ to convert from degree step to equatorial distance step and substituting $T_s/T_E = N/L$, where T_S and T_E are defined in Table 2. N and L are defined in Ref. [18]. $T_E^{\,c}$ is a constant.

Note: Definitions given in italics.
[a]Earth radius.
[b]Standard gravity.
[c]Earth rotational period.

Spatial resolution, $\overline{\Delta xy}$, is the square root of the product of the along-track and cross-track spatial resolutions of the wind measurements. It is made more coarse when downsampling to increase normalized standard deviation. Thus, we define spatial resolution as

$$\Delta xy = F_s \sqrt{\Delta x \Delta y}, \qquad (3)$$

where Δx and Δy are the cross-track and along-track spatial resolutions, respectively, defined in Table 2. F_s is the downsampling factor, each defined in Table 2. For this paper, we do not consider the use of postmeasurement resolution enhancement schemes.[19]

Daily coverage, C, is the fraction of the globe covered in a day. It is reduced by low inclination orbits, by operating for only part of the orbit, by gaps between subsequent passes,

Table 4 NSCAT and QuikSCAT performance as estimated by the solution space model and more detailed methods.

Response Dimension	NSCAT		QuikSCAT	
	Estimate	Detailed[a]	Estimate	Detailed[b]
K_{pc}	0.0038 to 6.0	0.001 to 4.0	0.045 to 0.050	0.005 to 0.5
N_L	4	4	10	2 to 4
Δxy (km)	35	12 to 35	4.2	13
C	0.84	0.89	1.0	1.0
T_r (hrs)	26	48	32	24

[a]NSCAT detailed performance values taken from Refs. 2 and 20.
[b]QuikSCAT detailed performance values taken from Refs. 21 and 22.

by gaps between subsequent scans, or by focusing on a single region while neglecting others. Thus, we approximate daily coverage as

$$C \approx \min\left(\frac{I_{\max}}{2/\pi}\frac{2W_s}{R_E\pi}, 1\right)\frac{D_o}{F_f} - \max\left(1 - \frac{2N_s[comp]W_s}{S} - a_y\frac{\omega T_s}{2\pi R_E}, 0\right), \qquad (4)$$

where $I_{\max}$ is the highest orbital inclination of any satellite in the constellation. I, F_f, and D_o are design parameters defined in Table 2. W_s and S are intermediate parameters defined in Table 3.

Revisit period, T_r, is the typical time between one pass and the next. We approximate it as

$$T_r \approx \frac{T_E W_s}{N_{op}S}, \qquad (5)$$

where T_E is the rotation period of the Earth. N_{op} is a design parameter, defined in Table 2. S and W_s are intermediate parameters defined in Table 3.

We verify the accuracy of the transformation between the design space and the response space by estimating the performance of the NSCAT and QuikSCAT scatterometers and comparing the estimates with detailed calculations of NSCAT and QuikSCAT performance taken from Naderi et al.,[2] Draper et al.,[21] the NSCAT User's Guide,[20] and the QuikSCAT User's Guide.[22] The estimates are obtained by transforming the NSCAT and QuikSCAT design parameters, given in Sec. 6, to the response space using the transformation approximations given above. The results are summarized in Table 4. In addition, the resulting intermediate parameters are provided for reference in Sec. 7.

Most of these estimates are within 50% of the values obtained through more detailed calculation, with the exception of QuikSCAT N_L and K_{pc}. We consider this suitable for an initial evaluation of the space of nonscanning designs.

4 Generating Measurement Concepts Using the Solution Space Model

We apply the solution space model to search for designs that may have become achievable in recent years. We identify alternative concepts for satellite wind scatterometry in those newly accessible design space regions. Other design applications may benefit from the solution space model, including system-wide optimization, trade-off analysis, and design parameter ranking, but are beyond the scope of this work.

In Sec. 4.1, we explore several advances that expand the design space and enable a greater capability-to-volume ratio, which supports a higher quantity of low-cost satellites. We explore several classes of cooperative modes for multiscatterometer constellations in Sec. 4.2.

In Secs. 4.3 and 4.4, we identify two new approaches to satellite wind scatterometry, with emphasis on CubeSat flocks and constellations. Despite their challenges, these concepts have the potential to significantly improve scatterometer performance on a variety of measures. For each concept, we briefly describe an example design, including key subsystems and the volume they consume, expressed in CubeSat units (U), which fill a 10 cm^3 volume and weigh 1.33 kg.

4.1 *Expansion of the Scatterometer Design Space*

Technology advances allow designs to be implemented with parameters that were previously outside the accessible design range. Compared to the 1990s and early 2000s when the traditional approaches to satellite wind scatterometry were developed, electronics are smaller, larger structures can be deployed, and launch can be shared by multiple small satellites. These advances have expanded the scatterometer design space, primarily by making it affordable to deploy multiple satellites (N_s) in multiple orbital planes (N_{op}) to observe the planet more frequently.

Mobile computing has driven mass production of miniaturized, low-power electrical components. This expands the accessible range of transmit power (P_t) as electronics consume less of the power budget and allow more space for power systems. Similar trends have expanded the range of possible bandwidths (B) and wavelengths (λ), but the complications of frequency allocations and the difficulty of developing the GMF at new frequencies make these advances beyond the scope of this work.

Advanced deployable mechanisms, including compliant[23,24] and origami-adapted[25] mechanisms, allow larger solar arrays and antennas to be stowed in a smaller volume for later deployment. This expands the accessible range of antenna length, (L_e), and transmit power, (P_t).

These advances increase satellite capability-to-volume ratio. Satellites can now be more capable for a given size or smaller for a given capability. This tradeoff favors smaller satellites. Satellite miniaturization is a compounding process, so capability-to-volume ratio may increase with miniaturization. For example, a smaller processing system that requires less power enables a smaller power system, which in turn allows for a smaller attitude control system, which consumes less power, etc. Smaller satellites cost less to build and less to launch, so more can be deployed in the same budget.

By launching on rideshare missions, the capabilities of a large, monolithic satellite can be divided among multiple, small satellites. In addition to providing increased capability-to-volume ratio, this creates an opportunity for redundant satellites instead of redundant components. Redundant components have unique interfaces, roughly equal to $m^2 n^2 / 2$, where m is the number of redundant multiples of each of the n components in the system. For example, a fully redundant power system must provide additional interfaces to each of the powered subsystems; must have an additional, unique, mounting interface; has additional, unique, impacts to navigation control, etc. Every unique interface brings with it added design and assembly work with added opportunities for design and assembly faults. For redundant satellites without redundant components, $m = 1$, which reduces unique interfaces to $n^2 / 2$, so redundant satellites have fewer interfaces by a factor of m^2. Redundant satellites may have better reliability with less complexity than a single satellite with redundant components. This further reduces cost, allowing more satellites to be deployed.

Satellite costs can also be reduced by subjecting components and assemblies to only those ground-based environmental tests that pass the expected value criterion: $\Delta \rho_e (C_S + C_L) > C_T$, where $\Delta \rho_e$ is the expected reliability increase, and C_S, C_L, and C_T are the costs of the satellite, launch, and ground test, respectively. If scatterometers are operated in very low orbits, which have relatively mild temperatures, mild radiation, and brief orbital life, much of space environmental testing can be safely traded for on-orbit testing.

For a constellation, these approaches allow new satellite designs to be prototyped in space sooner and lessons from space to be iterated upon more frequently. Reduced ground-based testing and more frequent deployments demonstrably enable rapid, low-cost improvement of small satellite constellations.[26,27]

4.2 *Co-Operative Modes*

Multiple satellites and antennas can be applied in a variety of cooperative arrangements, defined here as supplementary, complementary, and synergistic. The following descriptions apply to both satellites and antennas, but satellites alone are discussed for simplicity. Supplementary satellites ($N_s[sup]$) are interdependent satellites that work together to accomplish an objective, which they cannot accomplish alone. Complementary satellites ($N_s[comp]$) are independent, identical satellites that accomplish similar objectives without cooperation. Synergistic satellites
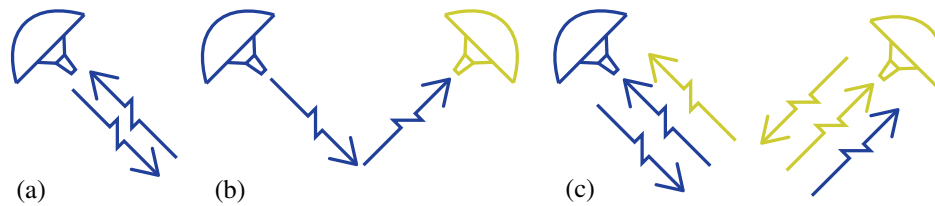
Fig. 4 Examples of co-operative radar modes. (a) Monostatic radar. (b) Simplex bistatic radar. (c) Full-duplex bistatic radar.

($N_s[syn]$) are cooperative, independent satellites that accomplish more together than they do individually.

Complementary satellites, demonstrated by contemporary scatterometers, take advantage of multisatellite redundancy and economies of scale without the risk of losing function due to failed modules. For example, RapidSCAT, a SeaWinds scatterometer that flew on the International Space Station for two years (2014 to 2015), and ASCAT were complementary for RapidScat's life. Together RapidSCAT and ASCAT demonstrated complementary co-operation, reducing gaps in wind vector coverage.

Supplementary and synergistic scatterometers may be operated in a variety of radar modes, which can be designated as monostatic or multistatic, simplex or duplex, half or full. The simplex/duplex and half/full designations apply only to multistatic radar and are adapted from the field of communications. Several examples of these radar modes are shown in Fig. 4.

The monostatic/multistatic designation indicates whether a signal is received by the instrument that transmitted it or by another, respectively. Figure 4(a) shows a monostatic radar, most common in scatterometry, which receives its own signal, scattered off the surface. Figures 4(b) and 4(c) are bistatic, a type of multistatic.

The duplex/simplex designation indicates whether instruments both transmit and receive or whether some transmit or receive only, respectively. Figure 4(b) shows a simplex bistatic radar system, in which a receiver measures the signal of a separate transmitter, scattered off the surface.

The half/full designation applies only to duplex radar and indicates whether observations are staged or simultaneous, respectively. If the radar instruments in Fig. 4(b) instead take turns transmitting while the other receives, they then form a half-duplex bistatic radar system. Figure 4(c) shows a full-duplex bistatic radar system, in which two radars simultaneously illuminate a target and measure the scatter from both signals. If the instruments in Fig. 4(c) instead alternate between simultaneous transmission and simultaneous reception, then this system becomes half-duplex bistatic.

Note that a single dual-pol antenna operating on a single platform is self-supplementary ($N_a[sup] = 2$) if the polarizations are operated in turns or self-synergistic ($N_a[syn] = 2$) if they are operated in tandem. Multiple single-pol antennas are complementary ($N_a[comp] = 2$) if used to expand the swath or supplementary ($N_a[sup] = 2$) if used to increase N_L.

4.3 *Supplementary Approach: Simplex Multistatic Scatterometer Flock*

Supplementary satellites can leverage compounding size reduction by separating the functions of a single scatterometer into modular segments. This is the motivation behind the simplex multistatic scatterometer flock, shown in Fig. 5. This approach might use a 3U CubeSat transceiver and downlink module to illuminate the surface, and multiple 1.5U CubeSat receiver modules with synchronized timing to observe the scattered signal from different azimuth angles. This architecture achieves the necessary N_L with a single antenna and no moving parts but requires formation flying. Multiple flocks can be combined into a larger constellation to provide global coverage and increase revisit rate.

For the 1.5U receiver modules, the receiver and bus electronics can be tightly packed into 0.5U. These may include a 10-W-h LiPo power system, magnetorquers, and integrated command and data handling, tasking telemetry and control, GPS-receiver for clock synchronization, and scatterometer receiver electronics. The remaining 1U is expected to be sufficient to stow an accordion-folded 1×0.1 m patch-array antenna.
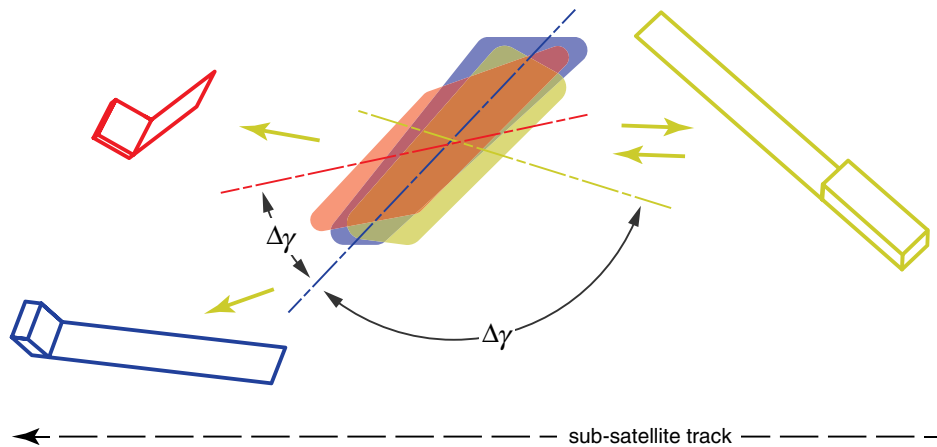
Fig. 5 Simplex multistatic scatterometer flock, consisting of a 3U Tx/Rx CubeSat and two, 1.5U Rx CubeSats, each with 1-m, fan-beam antennas. Together, the flock obtains the required three azimuth-diverse looks. Arrows illustrate unit transmit and receive functionality. $\Delta\gamma$ illustrates the azimuth diversity of the look directions. Ground footprints displacement is exaggerated for clarity.

For the 3U transceiver module, 0.75U is allocated for a flexible, deployable solar array providing roughly 150 W for radar and bus operation. Another 0.75U is allocated to the bus, the electronics for the radar transmitter, and additional LiPo power storage for eclipsed radar operations.

4.4 *Synergistic Approach: Full-Duplex Bistatic Scatterometer Pair*

Synergistic scatterometer co-operation allows each of several instruments to take advantage of the signal scattered by its companions in addition to its own. A full-duplex bistatic scatterometer approach, shown in Fig. 6, might include two identical scatterometers with synchronized timing. Pointing at the same region on the surface, they transmit in tandem, then receive in tandem. Assuming the signals are separable, each receives and demodulates its own signal as well as the signal of the other sensor.

This pairing produces two near-simultaneous, azimuth-diverse looks for each instrument, including one reverse scattering measurement for each (σ_{11}^0, σ_{22}^0) and one forward scattering measurement for each (σ_{12}^0, σ_{21}^0). While these four measurements do not constitute four azimuth-diverse measurements in the traditional sense, the forward scattering look geometry may add enough information to disambiguate the wind vector.

The subsystem breakdown is similar to that of the multistatic architecture 3U transceiver module, described in Sec. 4.3, except a wrap-around segment is added to the antenna to provide an additional meter of length for improved spatial resolution.
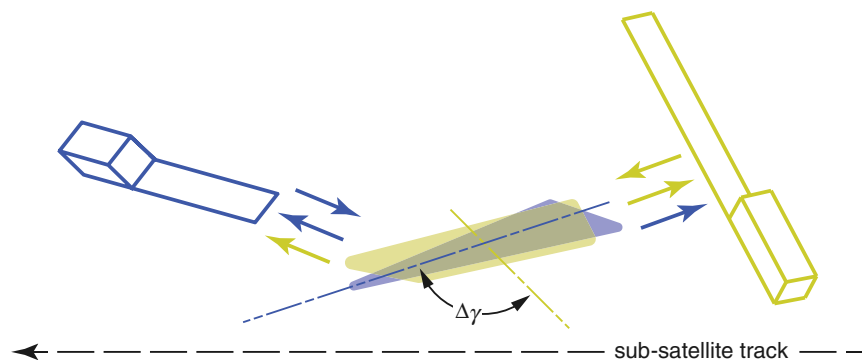
Fig. 6 Full-duplex bistatic scatterometer pair of two 3U Tx/Rx CubeSats with 2-m, fan-beam antennas, providing three to four azimuth-diverse looks (including backscatter and forward scatter). Arrows illustrate unit transmit and receive functionality. $\Delta\gamma$ illustrates the azimuth diversity of the look directions. Ground footprints displacement is exaggerated for clarity.

Table 5 Estimated performance of sample designs for CubeSat scatterometer constellations.

Response value	Simplex multistatic $N_{op} = 6,72$	Full-duplex bistatic $N_{op} = 6,72$	NSCAT (estimate)
K_{pc}	0.0017 to 7.8	0.0021 to 9.6	0.0038 to 6.0
N_L	3	3	4
$\overline{\Delta xy}$ (km)	24	24	35
C	0.7	0.7	0.84
T_r (h)	41, 3.4	41, 3.4	26

4.5 Estimated Performance Comparisons

The estimated performance of these architectures, using assumed constants close to those of NSCAT, is shown in Table 5. The NSCAT estimation is given for rough comparison. To achieve global ocean coverage, a constellation of six orbital planes, each with three flocks is considered for each concept. This comes to 54 satellites for the simplex multistatic case and 36 for the full-duplex bistatic case. However, since the total CubeSat flock is 6U in both cases, the total constellation volume comes out to 108U for both. Estimated performance of this constellation is comparable to that of NSCAT, with a slightly larger revisit.

To achieve more frequent revisit, a larger constellation of 72 orbital planes, each with three flocks, is considered. This comes to 648 satellites for the simplex multistatic case and 432 for the full-duplex bistatic case. Both cases total 1296U, which translates to 1723 kg of weight, compared to a weight of 870 kg for QuikSCAT.[28] Precedent has been established for satellite constellations with hundreds of satellites: Planet, Inc. recently constructed, launched, and commissioned roughly 300 satellites.[27] A constellation of scatterometers could give insight into near-hourly variations in wind (last row of Table 5), allowing researchers and forecasters to observe, model, and track the synoptic, mesoscale atmospheric processes that are not currently observable.

These constellation architectures have the potential to not only increase revisit rate but to decrease cost as well. Based on rough, order-of-magnitude cost investigation, a small constellation with performance equivalent to the traditional scatterometers could be built and launched for an order of magnitude less cost, on the order of O($10M) for a small CubeSat constellation versus O($100M) for a QuikSCAT replacement. A large constellation, on the order of O($100M), could be equivalent in cost to a traditional scatterometer, with an order of magnitude more frequent revisit.

5 Conclusion

We presented a parametric methodology for holistic evaluation of the solution space of a technology. We applied this methodology to model the solution space of satellite scatterometers by defining design parameters and response parameters and developing an approximate transformation between them. The transformation supports rapid evaluation of a variety of designs across the solution space. We verified the accuracy of the transformation using previous point designs, including NSCAT and SeaWinds on QuikSCAT, with results suitable for a first-look exploration of the design space. The solution space model may be useful for more comprehensive design optimization for satellite scatterometry. For example, a Monte Carlo analysis might be used to perform a screening experiment to determine the design parameters with the greatest statistical significance. The resulting, simplified solution space might be used to identify optimal designs for further simulation and development.

The solution space model provides insight into the potential of recent technologies to enable affordable constellations of co-operative CubeSat scatterometers for near-hourly measurement of ocean vector winds. We explored several concepts for co-operative satellite wind scatterometers and presented two example concepts. Further simulation and demonstration are needed to verify the expected performance of these approaches.

6 Appendix A: Design Values Used in Point Design Analyses

Table 6 provides input values used to develop the performance estimates given in Tables 4 and 5. Each design parameter is defined in Table 2. Table 4 compares performance estimates using the transformation model of Sec. 3.2 to those found through more detailed estimation. For this analysis, the input values come from the scatterometer user guides. To simplify modeling, we assume that all fan beams have similar geometry. As noted in Table 2, the effective antenna length is the antenna length multiplied by the antenna efficiency and square root of aperture efficiency. Although the antenna and satellite quantity parameters are split into subparameters, the default for each subparameter is one. For example, a single satellite has supplemental and complementary

Table 6 Design parameter input values used for estimating performance of scatterometers in Secs. 3.2 and 4.5.

Design parameter	NSCAT[2,20,29,30]	QuikSCAT[14,22,28]	Simplex multistatic	Full-duplex bistatic
Transmit power (W)	110	110	90	90
Pulse length (ms)	5	2	5	5
Radar duty cycle	0.309	0.378	0.3	0.3
Dwell time (ms)	125	5	540	540
Wavelength (cm)	2.14	2.24	2	2
Polarization (pol)	H, V	H, V	H	H
Bandwidth (kHz)	17 (Tx)	40 (Tx)	10	10
	400 (Rx)	250 (Rx)		
Look elevation angle (deg)	15.9 (min)	39.7 (inner)	15.9 (min)	15.9 (min)
	49.6 (max)	46.0 (outer)	49.6 (max)	49.6 (max)
Effective antenna length (cm)	8.08 (x)	90.0	9 (x)	9 (x)
	1.94 (y)		90 (y)	90 (y)
Orbit altitude (km)	795	803	795	795
Number of orbital planes	1	1	6, 72	6, 72
Orbit inclination (deg)	98.6	98.6	98.6	98.6
Orbit duty cycle	1.0	1.0	0.7	0.7
Satellite quantity	1	1	3 (comp)	3 (comp)
			3 (sup)	1 (sup)
			1 (syn)	2 (syn)
Antenna quantity	2 (comp)	1 (comp)	1	1
	4 (sup)	2 (sup)		
Focus factor	1	1	1	1
Scan angle (deg)	0	85.8 (x)	0	0
		85.8 (y)		
Sampling factor	120	1	120	120
Scan rotation rate (Hz)	0	1.50	0	0
Range of σ_0 values (dB)	−38 (min)	−37 (min)	−38 (min)	−38 (min)
	3 (max)	−7 (max)	3 (max)	3 (max)

antenna quantities of one each and supplementary, complementary, and synergistic satellite quantities of one each. Dual-polarized antennas are treated as two complementary antennas.

Table 5 presents initial performance estimates for the simplex multistatic and full-duplex bistatic CubeSat scatterometer constellations presented in Sec. 4. The solar power system required for 90-W transmit power at an orbit duty cycle of 0.7 are described in Sec. 4.3, as is the antenna system. Many parameters, such as pulse length, radar duty cycle, wavelength, bandwidth, look elevation angle, orbit altitude, orbit inclination, and scan parameters, are taken from NSCAT. The larger footprint allows for a longer dwell time. For each concept, a small constellation in six orbital planes and a large constellation in 72 orbital planes are presented in Sec. 4.5. The satellite and antenna quantities in each flock are described in Secs. 4.3 and 4.4. No scanning cases are considered. The value used for the downsampling factor of NSCAT, the Simplex multistatic, and the Full-duplex bistatic is an assumption, not drawn from actual NSCAT design parameters, that was selected to bring the NSCAT estimate in accordance with detailed calculation, as presented in Table 4. In addition to the design parameters, Table 6 includes the range of σ_0 values used in the analysis derived using the NSCAT model function.

7 Appendix B: Point Design Intermediate Parameters Resulting from Design Values

One of the benefits of the solution space model is it reduces the set of design parameters that the designer has to consider. Many parameters provide intuition but are not controlled by the designer. If the design basis is properly defined, these intermediate parameters are dependent on design parameters and constants. Thus, performance can be evaluated considering only the effects of the design parameters. The intermediate parameters can be ignored. However, to facilitate comparison with other systems, Table 7 gives the intermediate parameters estimated in the analyses that produced Tables 4 and 5. See Table 3 for definitions of each parameter.

Table 7 Intermediate parameter values from the point design analyses of Secs. 3.2 and 4.5.

Intermediate parameter	NSCAT	QuikSCAT	Simplex multistatic	Full-duplex bistatic
SNR	0.0087 (min)	5.0 (min)	0.00017	0.00017 (min)
	800 (max)	4900 (max)	2.07	2.07
Radar incidence angle (deg)	18 (min)	46 (inner)	18 (min)	18 (min)
	59 (max)	54 (outer)	59 (max)	59 (max)
Spatial resolution (km)	0.31 (x)	0.78 (x)	2.2 (x)	2.2 (x)
	8.5 (y)	30 (y)	17 (y)	17 (y)
dB beamwidth (deg)	13 (x)	1.3	11 (x)	11 (x)
	0.56 (y)		1.1 (y)	1.1 (y)
Earth angle (deg)	2.1 (min)	6.3 (min)	2.1 (min)	2.1 (min)
	9.4 (max)	8.1 (max)	9.4 (max)	9.4 (max)
Slant range (km)	740 (min)	970 (min)	738 (min)	738 (min)
	1200 (max)	1100 (max)	1200 (max)	1200 (max)
Footprint width (km)	327 (x)	23 (x)	270 (x)	270 (x)
	8.5 (y)	30 (y)	17 (y)	17 (y)
Antenna footprint area (km^2)	2800	667	4712	4712
Swath width (km)	2631	2100	276	276
Rescan window (min)	2.6	2.3	2.6	2.6
Satellite velocity (km/s)	7.5	7.5	7.5	7.5
Satellite orbital period (min)	100	100	100	100
Satellite orbit step (m)	2800	2800	2800	2800

Acknowledgments

References

1. F. T. Ulaby and D. G. Long, *Microwave Radar and Radiometric Remote Sensing*, University of Michigan Press, Ann Arbor (2013).
2. F. Naderi, M. Freilich, and D. Long, "Spaceborne radar measurement of wind velocity over the ocean-an overview of the NSCAT scatterometer system," *Proc. IEEE* **79**(6), 850–866 (1991).
3. D. G. Long, "Polar applications of spaceborne scatterometers," *IEEE J. Sel. Top. Appl. Earth Obs. Remote Sens.* **10**(5), 2307–2320 (2017).
4. H. Stephen, D. Long, and P. Hardin, "Vegetation study of Amazon using QSCAT in comparison with SASS, ESCAT, and NSCAT," in *Proc. Int. Geosci. and Remote Sens. Symp.*, pp. 429–431 (2000).
5. D. B. Lindell and D. G. Long, "High-resolution soil moisture retrieval with ASCAT," *IEEE Geosci. Remote Sens. Lett.* **13**(7), 972–976 (2016).
6. H. Stephen and D. Long, "Surface statistics of Saharan sand dunes derived from scatterometer measurements," in *Proc. Int. Geosci. and Remote Sens. Symp.*, pp. 1549–1551 (2003).
7. National Academies of Sciences and Engineering, and Medicine, *Thriving on Our Changing Planet: A Decadal Strategy for Earth Observation from Space*, National Academies Press, Washington, DC (2018).
8. W. Lin and X. Dong, "Design and optimization of a Ku-band rotating, range-gated fanbeam scatterometer," *Int. J. Remote Sens.* **32**(8), 2151–2171 (2011).
9. W. Tsai et al., "Postlaunch sensor verification and calibration of the NASA scatterometer," *IEEE Trans. Geosci. Remote Sens.* **37**, 1517–1542 (1999).
10. H. Hersbach, A. Stoffelen, and S. de Haan, "An improved C-band scatterometer ocean geophysical model function: CMOD5," *J. Geophys. Res. Oceans* **112**(C3), C03006 (2007).
11. H. J. Kramer, "Skylab space station," https://directory.eoportal.org/web/eoportal/satellite-missions/s/skylab (accessed 1 July 2019).
12. H. J. Kramer, "SeaSat mission—the world's first satellite mission dedicated to oceanography," https://directory.eoportal.org/web/eoportal/satellite-missions/s/seasat (accessed 1 July 2019).
13. H. J. Kramer, "ERS-1 (European remote-sensing satellite-1)," https://directory.eoportal.org/web/eoportal/satellite-missions/e/ers-1 (accessed 15 July 2018).
14. M. Spencer, C. Wu, and D. Long, "Tradeoffs in the design of a spaceborne scanning pencil beam scatterometer: application to SeaWinds," *IEEE Trans. Geosci. Remote Sens.* **35**(1), 115–126 (1997).
15. J. Figa-Saldaña et al., "The advanced scatterometer (ASCAT) on the meteorological operational (MetOp) platform: a follow on for European wind scatterometers," *Can. J. Remote Sens.* **28**(3), 404–412 (2002).
16. C. A. Mattson and C. D. Sorensen, *Fundamentals of Product Development*, CreateSpace Independent Publishing Platform, Provo, Utah (2015).
17. M. A. Richards, J. A. Scheer, and W. A. Holm, *Principles of Modern Radar*, Scitech Publishing Inc. (2015).
18. C. Elachi and J. van Zyl, *Introduction to the Physics and Techniques of Remote Sensing*, 2nd edn., John Wiley & Sons, Inc. (2006).
19. D. Long, "Comparison of SeaWinds backscatter imaging algorithms," *IEEE J. Sel. Top. Appl. Earth Obs.* **10**(3), 2214–2231 (2017).
20. "NSCAT science data product user's manual," Jet Propulsion Laboratory, California Institute of Technology, Vol. 1.1 (1997).

21. D. W. Draper and D. G. Long, "Simultaneous wind and rain retrieval using SeaWinds data," *IEEE Trans. Geosci. Remote Sens.* **42**(7), 1411–1423 (2004).

22. "QuikSCAT science data product user's manual," T. Lungu, Ed., Jet Propulsion Laboratory, California Institute of Technology, Vol. 3.0 (2006).

23. R. Fowler, L. Howell, and S. Magleby, "Compliant space mechanisms: a new frontier for compliant mechanisms," *Mech. Sci.* **2**(2), 205–215 (2011).

24. B. DeFigueiredo, S. Magleby, and L. Howell, "Flexible and conformal electronics using rigid substrates," U.S. Patent 650453 (2018).

25. S. A. Zirbel et al., "Hanaflex: a large solar array for space applications," *Proc. SPIE* **9467**, 94671C (2015).

26. C. Boshuizen et al., "Results from the Planet Labs flock constellation," in *Proc. AIAA/USU Conf. Small Satell.*, Vol. 28, American Institute of Aeronautics and Astronautics (AIAA) (2014).

27. R. Zimmerman et al., "Comissioning the world's largest satellite constellation," in *Proc. AIAA/USU Conf. Small Satell.*, Vol. 31, American Institute of Aeronautics and Astronautics (AIAA) (2017).

28. D. Steitz et al., "QuikSCAT scatterometer press kit," National Aeronautics and Space Administration (1999).

29. F. J. Wentz and D. K. Smith, "A model function for the ocean-normalized radar cross section at 14 GHz derived from NSCAT observations," *J. Geophys. Res. Oceans* **104**(C5), 11499–11514 (1999).

30. D. G. Long, C.-Y. Chi, and F. Li, "The design of an onboard digital Doppler processor for a spaceborne scatterometer," *IEEE Trans. Geosci. Remote Sens.* **26**(6), 869–878 (1988).

31. M. P. Walton and D. G. Long, "Architectures for Earth-observing CubeSat scatterometers," *Proc. SPIE* **10769**, 1076904 (2018).

Patrick Walton is pursuing his MS degree in electrical and computer engineering at Brigham Young University (BYU). He received his BS degree in mechanical engineering with university honors from BYU in 2017. He is a cofounder of Care Weather Technologies, an up-and-coming developer of nanosatellites for weather observation. Previously, he was the system engineer and project lead for BYU's Passive Inspection CubeSats mission, which uses two 1U CubeSats to capture images of a launch vehicle.

David Long worked at NASA's Jet Propulsion Laboratory (JPL) on advanced radar remote sensing systems and scatterometer projects. He is a professor in the Electrical and Computer Engineering Department at Brigham Young University where he teaches upper division and graduate courses in communications, microwave remote sensing, radar, and signal processing. He is the director of the BYU Center for Remote Sensing. He has over 400 publications in signal processing, radar scatterometry, and synthetic aperture radar.